the perceived size of the defect. Current research is aimed at quantifying this effect.

CONCLUSION

This study confirms earlier work showing that segmental defect sizes are underestimated, particularly in the right lower lobe. Although there was fair intraobserver agreement in reporting such defects, the accuracy of estimation was 50%. The variability and inaccuracy might be reduced by the use of a guide to segmental anatomy. This virtual scintigraphic model of lung anatomy allows the study of minimal perceptible defect size and how this varies with the location of the defect in the lungs. Such issues are currently under investigation.

ACKNOWLEDGMENTS

REFERENCES

1. PIOPED Investigators. Value of the ventilation/perfusion scan in acute pulmonary embolism. Results of the prospective investigation of pulmonary embolism diagnosis (PIOPED). *JAMA* 1990;263:2753-2759.
2. Gottschalk A, Juni JE, Sostman HD, et al. Ventilation-perfusion scintigraphy in the PIOPED study. Part I. Data collection and tabulation. *J Nucl Med* 1993;34:1109-1118.
3. Gottschalk A, Sostman HD, Coleman RE, et al. Ventilation-perfusion scintigraphy in the PIOPED study. Part II. Evaluation of the scintigraphic criteria and interpretations. *J Nucl Med* 1993;34:1119-1126.
4. Sostman HD, Coleman RE, DeLong DM, Newman GE, Paine S. Evaluation of revised
criteria for ventilation-perfusion scintigraphy in patients with suspected pulmonary embolism. *Radiology* 1994;193:103-107.
5. Morrell NW, Nijran KS, Jones BE, Biggs T, Seed WA. Underestimation of segmental defect size in radionuclide lung scanning. *J Nucl Med* 1993;34:370-374.
6. Zubal IG, Harrell CR, Smith EO, Rattner Z, Gindi G, Hoffer PB. Computerized three-dimensional segmented human anatomy. *Med Phys* 1994;21:299-302.
7. NM/MIRD. *Estimates of specific absorbed fractions for photon sources uniformly distributed in various organs of a heterogeneous phantom,* vol. 5. New York: Society of Nuclear Medicine; 1978.
8. Magnussen J, Chicco P, Vu D, et al. Study of sectional segmental anatomy of the human lung using gelatin embedded sections and CT imaging techniques [Abstract]. *Proceedings of the 1996 Conference of the Anatomical Society of Australia and New Zealand.* 1996:22.
9. Netter FH, Colacino S, eds. *Atlas of human anatomy.* Basel, Switzerland: Ciba-Geigy; 1989.
10. Gray H, Williams PL, Warwick R, et al., eds. *Gray's anatomy,* 37th ed. Edinburgh: Churchill Livingstone; 1989.
11. Agur AMR, Lee MJ, Gardner JN, eds. *Grant's atlas of anatomy,* 9th ed. Baltimore: Williams and Wilkins; 1991.
12. Lewellen TK, Anson CP, Haynor DR, et al. Design of a simulation system for emission tomographs [Abstract]. *J Nucl Med* 1988;29:871.
13. Haynor DR, Harrison RL, Lewellen TK. The use of importance sampling techniques to improve the efficiency of photon tracking in emission tomography simulations. *Med Phys* 1991;18:990-1001.
14. Morrell NW, Roberts CM, Jones BE, Nijran KS, Biggs T, Seed WA. Anatomy of radioisotope lung scanning. *J Nucl Med* 1992;33:676-683.
15. Cohen J. Weighted kappa: nominal scale agreement with provision for scaled disagreement or partial credit. *Psychol Bull* 1968;70:213-220.
16. Carbonell AM, Landis GA, Miale A, Moser KM. Construction and testing of a thorax-lung phantom to aid in scintiphotograph interpretation. *Invest Radiol* 1969;4:275-285.
17. Moser KM, Harsanyi P, Rius-Garriga C, Guisan M, Landis GA, Miale A. Assessment of pulmonary photoscanning and angiography in experimental pulmonary embolism. *Circulation* 1969;39:663-674.
18. Boyden EA. Segmental anatomy of the lungs: a study of the patterns of the segmental bronchi and related pulmonary vessels. New York: McGraw-Hill, 1955.
19. Landis JR, Koch GG. The measurement of observer agreement for categorical data. *Biometrics* 1977;33:159-174.

Effect of Registration Errors Between Transmission and Emission Scans on a SPECT System Using Sequential Scanning

Craig D. Stone, James W. McCormick, David R. Gilland, Kim L. Greer, R. Edward Coleman and Ronald J. Jaszczak

Department of Radiology, Duke University Medical Center, Durham, North Carolina

The purpose of this study was to evaluate the effects of patient motion on nonuniform attenuation correction of cardiac SPECT when the transmission and emission scans were performed sequentially. By using a sequential protocol rather than doing the scans simultaneously, contamination from the emission scan into the transmission scan could be eliminated, but registration of the two scans become a concern. **Methods:** Transmission and emission scans were acquired using both an anthropomorphic thorax phantom containing a cardiac insert and a human volunteer. The types of motion considered were transverse shifts, axial shifts and rotations that occur in the time period between the transmission and emission scan. For this study, the various types of motion were simulated in the data. Both the transmission and emission data were reconstructed using filtered backprojection. A single-iteration Chang algorithm, modified for nonuniform attenuation correction, was used to further process the emission data. To evaluate the effects of motion errors, circumferential profiles, all normalized to the same scale, were generated for each case. The cardiac images reconstructed using registered data were considered references. Error profiles were generated by subtracting misaligned images from the reference and then normalizing the difference by the reference. For comparison purposes, an error profile was generated for the case in which no attenuation correction was performed. **Results:** It was found that, for transverse and axial shifts of 2.9 cm, the normalized myocardial SPECT activity was decreased in certain regions of the heart by 20%-35%. For a 12° rotational shift, the error was on the order of 10%-20%, compared to a normalized variation of 20%-25% in the image with no attenuation correction. **Conclusion:** The results indicate that registration errors of 2-3 cm can seriously affect image quality in both the phantom and human images.

Key Words: SPECT; registration; sequential scan; transmission scan; emission scan

A major problem limiting the qualitative and quantitative accuracy of cardiac SPECT is photon attenuation. Compensation techniques that assume constant attenuation coefficients are inadequate for the thorax because of nonuniform attenuation (*1,2*). Various methods to correct for nonuniform attenuation have been proposed (*1-7*), none of which provide an exact analytical solution to the problem. Most of these techniques

require that a transmission CT scan be obtained, either simultaneously or sequentially, along with the SPECT scan. The acquired transmission CT data are used to generate a map of attenuation coefficients for emission image correction. One suggested protocol for obtaining both transmission CT and SPECT data on a multiheaded SPECT camera involves performing a fast fanbeam transmission scan (2–3 min), followed by a conventional emission scan (3). Sequential scanning has both advantages and disadvantages, compared with the simultaneous method. Simultaneous acquisition can result in contamination of data by improperly detected photons and decreased sensitivity of the emission data. Sequential acquisition can increase both scan time and the likelihood of misregistration between transmission and emission data. Misregistration can also occur in simultaneous scans if one or more of the detectors is misaligned, although the degree of misregistration considered in this study (up to ~3 cm) is not likely to occur with misaligned heads. The purpose of this study was to consider the effects of misregistration.

Much of the previous work in image registration considered the problem of correlating images from different modalities, such as CT or magnetic resonance imaging (8–12). The ability to acquire both transmission and emission SPECT scans has only recently become available commercially. In the case of PET, the problem of misregistration between sequential transmission and emission scans has been examined in some detail (13–15). For PET, an exact method exists for nonuniform attenuation correction (disregarding noise and measurement errors) if the sinogram of attenuation correction factors is known. Because of sharp boundaries between the lungs and soft tissue in the thorax, misalignment errors will cause significant quantitative errors and changes in regional myocardial activity (13). In SPECT, most myocardial studies are evaluated based on qualitative criteria. In this study, we are interested in the normalized (relative) quantitative effects of motion errors on the reconstructed myocardial image rather than on absolute quantitative effects. The evaluated motions for scan misregistration include x, y and z translations and axial rotations. The data demonstrate the nature of the movement-induced image artifacts that can be produced.

The method used for nonuniform attenuation correction in SPECT affects the final results. For this study, filtered backprojection was used to reconstruct the transmission and emission images. The iterative Chang algorithm (16), modified for nonuniform attenuation correction, was then applied to the emission image. Transmission and emission scans, using both a thorax phantom and a human patient, were acquired to evaluate misregistration.

MATERIALS AND METHODS

The phantom experiment was conducted with an anthropomorphic thorax phantom (ECT/TOR/P; Data Spectrum Corp., Hillsborough, NC). The phantom measured 38 × 26 cm and contained two lung inserts, a liver insert, a Teflon spine and a removable cardiac insert (ECT/CAR/I; Data Spectrum Corporation, Hillsborough, NC). The two lung inserts contained Styrofoam beads and were filled with water to simulate the density of lung tissue (0.049 cm^{-1}, as measured using narrow-beam transmission). The cardiac insert contained a ventricle and myocardial chamber. Each chamber could be filled separately with activity.

Three set of experiments were performed with the phantom. In Experiment 1 (Fig. 1A), the heart insert was positioned in the thorax phantom, with an approximately 2-cm space between the edge of the heart and the lung boundary. In Experiment 2 (Fig. 1B), the lung size was increased by attaching bags filled with Styrofoam

beads and water to the exterior of the lung inserts. The heart was contiguous with the inserted bag for most of its length. In Experiment 3 (Fig. 1C), the bags were removed, and the heart insert was rotated so that an area near the apex of the heart was contiguous with the lung boundary of the phantom. There were two reasons for measuring the three different geometries. The first involved determining the effect of the heart/lung geometry on the magnitude and nature of the registration errors. The second reason was to obtain average results, to better simulate patient variability.

A human patient was then examined in an attempt to replicate the earlier results. This patient, a 43-yr-old woman, was chosen because her body size made it possible to obtain transmission CT scans without the confounding effects of truncation. Thus, if the results from this human subject did not concur with the phantom results, then it could be surmised that the results obtained from the phantom were not applicable to humans. This patient gave prior written informed consent, which was in compliance with standards set by Duke University Medical Center.

Acquisition

The data were acquired on a three-headed SPECT system (Trionix Research Laboratories, Inc., Twinsburg OH). The phantom was placed so that the center was approximately along the axis of rotation for the gantry. A line-source assembly (3) was mounted on the gantry of the SPECT system opposite one head (Fig. 2). During the transmission scan, the line source was set with an air attenuator, whereas a transmission reference image would be acquired with the line source set to a copper attenuator to minimize dead time. A multislat collimator was mounted on the line source, and a fanbeam collimator (Nuclear Fields, Inc., Des Plaines, IL) was mounted on head one of the Triad system. A detailed description of the multislat collimator has been provided previously (3). The fanbeam collimator had a focal length of 114 cm (measured to crystal surface), a thickness of 4 cm, hexagonal holes that were 0.25 cm, edge-to-edge and a septal thickness of 0.025 cm.

The transmission scans for each phantom experiment were performed without any activity in the phantom. A line source, 27 cm long, containing between 1705 MBq and 2410 MBq (46.1–65 mCi) of ^{99m}Tc pertechnetate was used for the experiments.

To avoid truncation of the thorax phantom in the transmission acquisition, a two scan method was used that created a larger field of view (17,18). The phantom was mounted in a fixture that allowed accurate x-axis translation (Fig. 2A). In Scan 1, the phantom was shifted from the axis of rotation in the x direction by −4.8 cm, whereas in the second scan, the phantom was shifted in the x direction by +4.8 cm. For both scans, the detector was positioned at a radius of rotation of 30.2 cm (measured to detector crystal). With the system's actual field of view of 29.8 cm, the effective field of view was 39 cm, after the phantom was shifted, as outlined above. The data from the two shifted scans were reconstructed with previously developed software (17). The data were acquired for 90 min using a matrix size of 128 × 64 pixels (3.56 mm pixel size) and a 3° angular sampling with step-and-shoot gantry motion through a complete 360° range. We obtained human transmission CT scans using acquisition time, ranging from 2 to 20 min. Therefore, the phantom transmission CT scans have between 4.5 and 25 times the number of counts as our human scans. A 15% centered energy window (130 keV $\leq E_\gamma \leq$ 151 keV) was used for the transmission CT acquisitions. A planar reference image was taken for 600 sec. The center of the phantom was in the field of view for both scans, so that the noise was reduced in the region of the heart insert.

The location of the phantom in the scanner was accurately marked using a laser positioning system. Because we were interested in systematic errors caused by misregistration, very high
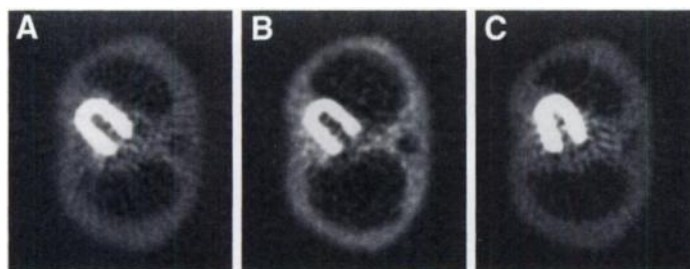
FIGURE 1. Images of the phantom showing the registered position of the heart for Experiment 1 (A), Experiment 2 (B) and Experiment 3 (C).

count transmission and emission studies were performed to collect the necessary data for analysis. The myocardium was filled with 0.64 MBq/ml (17 μCi/ml) ^{99m}Tc-pertechnetate (total myocardial volume was 120 ml). To simulate background activity, the main chamber of the thorax was filled with 0.028 MBq/ml ^{99m}Tc-pertechnetate. These concentrations produced a ratio of approximately 20:1 (19). The phantom was then carefully repositioned using the laser positioning system.

Low-energy, high-resolution parallel-hole collimators were used to acquire the emission data. The low-energy, high-resolution collimators had a sensitivity of 135 hertz/MBq and a resolution (FWHM) of 8.4 mm at 10 cm from the collimator surface.

For the emission scans the matrix size, angular sampling and primary energy window were set identically to the transmission scan. In addition, a scatter window was used (90 keV $\leq$ E$_\gamma$ $\leq$ 128 keV), and the total scan time was increased to 120 min. The activity was about eight times greater than would be present in a clinical scan, and the scanning time was six times that of the typical clinical scan (20). The increased counts reduced the effects of Poisson noise in the scans.

The transmission CT scan for the patient was performed in a similar manner. The main difference was due to the small body size; this allowed transmission CT data to be acquired with one scan. No activity was in the patient during the scan. Technetium-99m-pertechnetate (5069 MBq, or 137 mCi) was placed in the line source. Note that the patient was not exposed to the full effects of ^{99m}Tc because the radiation passed through a slat collimator that attenuated the beam significantly. For this scan, the data were acquired for 20 min using a matrix size of 128 $\times$ 128 pixels (3.56 mm pixel size) and a 3° angular sampling with step-and-shoot gantry motion through a complete 360°. Again, a 15% centered energy window (130 keV $\leq$ E$_\gamma$ $\leq$ 151 keV) was used for the transmission CT acquisitions. A planar reference image was also taken for 600 sec. After the transmission CT scan, the patient was injected with 299 MBq (8.08 mCi) of ^{99m}Tc-sestamibi during an exercise stress test. Afterward, the patient was repositioned using the laser positioning system.

Low-energy, ultra-high-resolution parallel-hole collimators were used to acquire the emission data for the human patient. The low-energy, ultra-high-resolution collimators had a sensitivity of 80 counts/sec/MBq and a resolution (FWHM) of 6.2 mm at 10 cm from the collimator surface.

For the emission scans, the matrix size, angular sampling, primary energy window and scatter energy window were set at the same values as those in the phantom emission study. However, the patient scan time was restricted to 20 min, as opposed to 120 min.

Preprocessing and Image Reconstruction

Because of the length of the transmission and emission scans for the phantom studies, the projection data were scaled to correct for radioactive decay of the emission source. Such a scaling of the data meant that the data were no longer Poisson distributed; however, the noise level was low enough to justify the procedure. Before
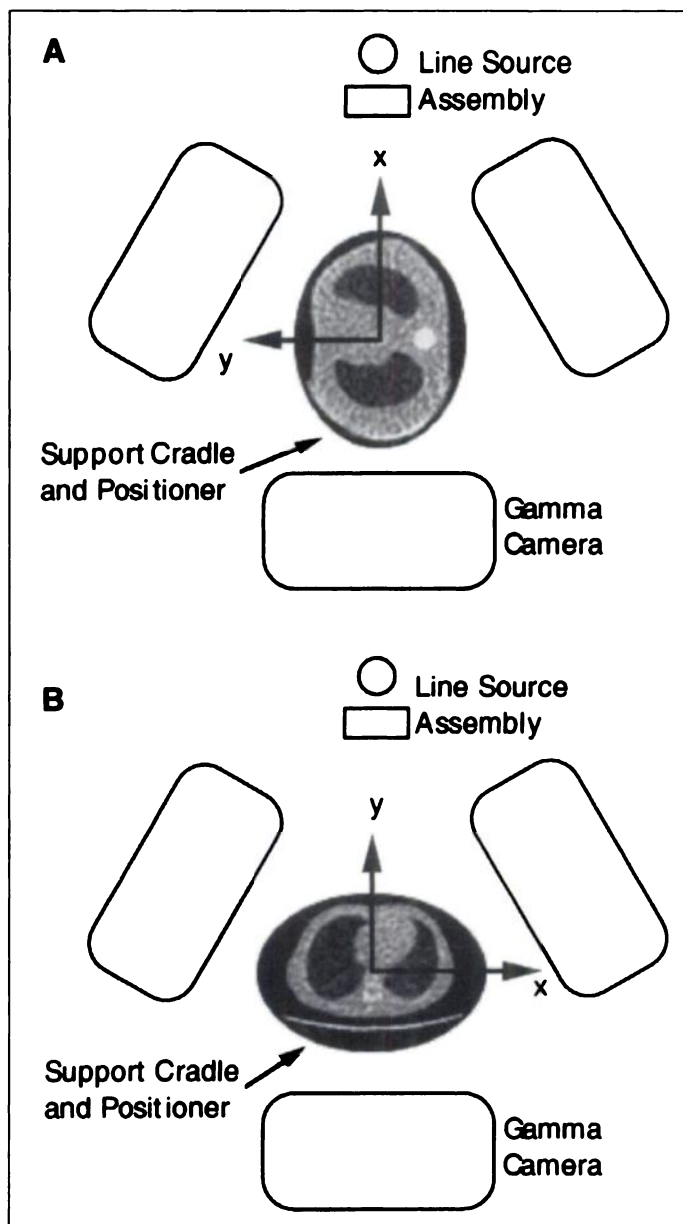

FIGURE 2. Orientation of the phantom in the SPECT system along with the coordinate system (A). Orientation of the human patient along with the coordinate system (B).

reconstruction, the measured transmission data were converted to line integrals of linear attenuation by taking the natural logarithm of the ratio of the incident reference image to the measured transmission projection data. Before the logarithm was taken, the reference image was scaled to account for the differences in acquisition time and decay between the reference and the transmission data.

The data were reconstructed using the filtered backprojection algorithm. The reconstructed images were filtered with a two-dimensional Butterworth filter with cutoff frequencies ranging from 0.702 to 0.843 cycles/cm (50%–60% of the Nyquist frequency) and order n = 5. For the emission data, nonuniform attenuation correction was performed using the modified iterative Chang algorithm (16,21–23). The modification involved taking the nonuniform attenuation factors into account. In this form, each pixel in the initial filtered backprojection reconstruction is multiplied by a correction term that is related to the average attenuation for that pixel. Thus, the correction term for pixel i, j could be written as:

$$C(i,j) = \cfrac{1}{\cfrac{1}{M}\sum_{m=1}^{M}\exp\left[-\sum_{i'\in I_{ijm}}\sum_{j'\in J_{ijm}}\mu(i',j')d(i',j',m)\right]}, \quad \text{Eq. 1}$$

where M is the number of angles; I_{ijm} and J_{ijm} are the set of i and j indices, respectively, of pixels intersected along the path of the detector at angle m; $\mu(i,j)$ is the attenuation coefficient distribution; and d(i,j,m) is the pathlength through pixel i,j at angle m. This first-order corrected image is then reprojected in such a way that models attenuation, based on the specified attenuation coefficient distribution. The reprojection is subtracted from the original data to generate error projections. An error image is then reconstructed by filtered backprojection and each pixel in the error image is multiplied by the corresponding correction term. The error image is then added to the first-order corrected image to generate the single iteration image (23). The emission data were also scatter-corrected using the dual-window subtraction method (22,23). A scatter coefficient of 0.3–0.35 was used, which generated an image in which the average counts in the lung were close to zero.

Motion Simulation

Figure 2A shows the coordinate system used for the object space of the system with the phantom. Note that the phantom cradle was designed to position the thorax phantom with its major axis (defined as the x-axis) aligned in the vertical direction. The patient data (Fig. 2B) were acquired with the major axis (x-axis) of the patient aligned in a horizontal direction. The axis of rotation for the gantry is the z-axis. The modified Chang algorithm was executed as a postprocessing step to the reconstruction. A translation of the attenuation map would have the identical effect to a physical translation of the object between transmission and emission scans (as long as the entire object remained in the field of view). Thus, translations in the x, y and z directions were simulated by shifting the attenuation map. Rotations around the z-axis were simulated by reordering the emission projection data and then reconstructing the new projection set.

Figure 1 shows the orientation of the heart insert in the thorax phantom for a typical slice in the case in which the transmission and emission images were registered. For translation, images were generated with 2 pixel shifts along each axis. These shifts ranged from −8 to 8 pixels (−2.9–2.9 cm). Rotation was performed in 3° increments that extended from −12° to +12°.

Only axial rotations were considered because the degrees of rotation in other directions would not be much of a factor. Rotation around the x-axis is very unlikely because it would require the table on which the patient lies to have some kind of rotation. Given a properly operating table, this is not likely. The other type of rotation not studied is rotation about the y-axis. The rotational errors introduced by repositioning a person between scans will be very small (typically <1°).

Analysis

The misaligned data were evaluated by converting the short-axis slices of the heart to circumferential profiles (a Mercator plot of the heart) using Trionix software. In all cases, the peak pixel within the cardiac region was normalized to 100, and the remaining pixels were normalized to a relative scale that extended from 0 to 100. In the human data, only counts within the myocardium were used for computing the normalization because other regions of the thorax contained high counts. The pixel dimensions of the Mercator plot are 50 × 160. The strip corresponds to 24 short-axis slices. A profile, 10 pixels high, was taken through the center of the strip. Thus, data from the apex and base of the heart were not included. This middle region was chosen because the Mercator plot magnifies the upper and lower contours of the object in study. For

Experiment 3, because the apical tip of the cardiac insert is next to the lung boundary, we expected that this phantom would experience larger errors than would the other phantoms in the study. These errors would be greatest when the apical region was initially in the lung, with smaller increases in error occurring in the middle region of the cardiac region. Counts were summed across the 10 pixels and recorded along the horizontal length of the strip (Fig. 3A). The profile height was equivalent to about five short-axis slices. The normalized error for the profile was calculated using the following expression:

$$\% \text{ error} = 100 \times (\text{misaligned} - \text{aligned})/\text{aligned}, \quad \text{Eq. 2}$$

where aligned refers to the registered, attenuation-corrected myocardial images and misaligned refers to the misaligned image. Because both sets of Mercator plots were normalized separately, the calculated error measured the relative change between the aligned and unaligned plots. For comparison, Figure 3B plots the normalized error for a Mercator plot in which no attenuation correction was performed (in Eq. 2, the misaligned image was replaced with the uncorrected image). Pixels 0–40 correspond to the anterior wall, 40–80 to the septal wall, 80–120 to the inferior wall and 120–160 to the lateral wall.

RESULTS

Phantom

For the three sets of phantom data, the four types of motion were simulated. For each type of motion, the errors were averaged over the three experiments. Figure 4 shows the average normalized error curves for x-axis and y-axis translation. A positive x-axis shift of the emission data with respect to the attenuation map would be equivalent to the patient moving left horizontally between transmission and emission scans. This may be simulated by moving the attenuation map in the opposite direction. For a negative shift, the error was relatively small, under 10% for most of the profile (Fig. 4B). With this type of shift, the heart would remain in soft tissue. The errors associated with a positive shift were substantially larger. A 2.9-cm positive shift decreased the activity in the anterior and lateral sections of the myocardium by more than 25%, and there was a slight increase in the septal section (Fig. 4A). The error was as great as the maximum error for the uncorrected image. The fact that the errors were nonuniform around the circumference of the heart is of great importance for qualitative analysis of the images. With positive x-axis shifts, the heart will cross into the lung, which has a narrow-beam attenuation coefficient value of 0.049 cm^{-1} compared with a soft tissue value of 0.153 cm^{-1}. Crossing of the lung boundary is most likely responsible for the qualitative and quantitative difference in the error curves.

The effect of y-axis translation of the phantom is displayed in Figure 4C and D. Such a motion could be caused by vertical movement of the bed. An upward shift between scans would correspond to a positive y-axis shift. For a positive shift of the emission data, there was a marked decrease in activity in the septal and inferior walls of the myocardium (Fig. 4C). The activity in the lateral wall changed very little. For a negative shift, the effects on the different segments of the heart were reversed, with marked decreases in activity in the anterior and lateral segments and a 5% increase in the septal area (Fig. 4D).

The results from z-axis motion are shown in Figures 5A and B. This type of motion would correspond to the patient sliding in or out of the gantry. It could also be caused by cardiac creep, a phenomenon that can occur after cessation of vigorous exercise (24). In this study, the thorax phantom was oriented in the gantry head first. A positive shift would have the patient
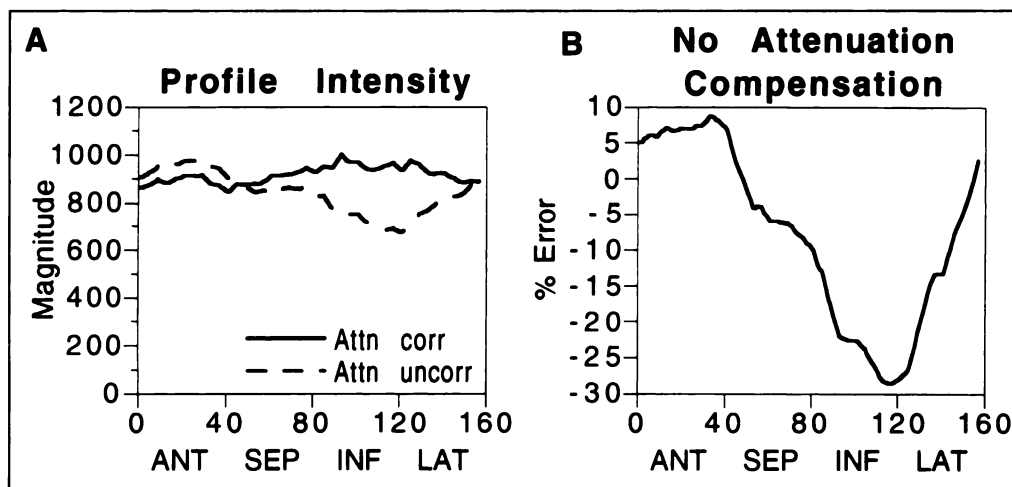
FIGURE 3. A 10-pixel-wide profile for the phantom of the attenuation-corrected and uncorrected Mercator plots (A). Plot of the normalized error for the case in which no attenuation correction was performed on the phantom SPECT image (B).

moving away from the gantry. The maximum errors were associated with negative shifts. The differences between the two directions were not as pronounced as those with the x-axis or y-axis because of the largely parallel motion of the heart relative to the lung boundary. The largest error occurred between the inferior and lateral sections with a 2-cm shift generating a 16% decrease in activity. The large errors also extend into the anterior segment (Fig. 5B). A negative shift would move the heart up in the chest. In the phantom, the lungs are larger toward the top. Thus, a negative shift would move the heart closer to the lung boundary. The errors associated with a positive shift, although smaller, were still significant (Fig. 5A).

Figure 5C and D, illustrate the effect of rotations. A positive rotation of the emission data with respect to the attenuation map would correspond to a counterclockwise rotation of the patient. For both positive and negative rotations, the errors were small compared to translational errors. Clockwise rotations caused a decrease in the anterior and lateral segments and a small increase in the septum-posterior segments. For counterclockwise rotations, there was a fairly small decrease in the septal region of the heart. The relatively small changes in activity caused by rotations can most likely be explained by the way the Chang algorithm calculates a correction factor for each pixel (Eq. 1). An average of inverse attenuation factors measured from the pixel to the detector at many angles was used to compute the correction factor. For an object near the center of the thorax, such as the heart, rotating the image by a small angle would probably not have a major effect on this average. Rotations that do not occur on the axis of rotation will likely increase the error observed here. As the rotations take place farther away from the axis of rotation for the gantry, the cardiac region starts experiencing both x and y translations with respect
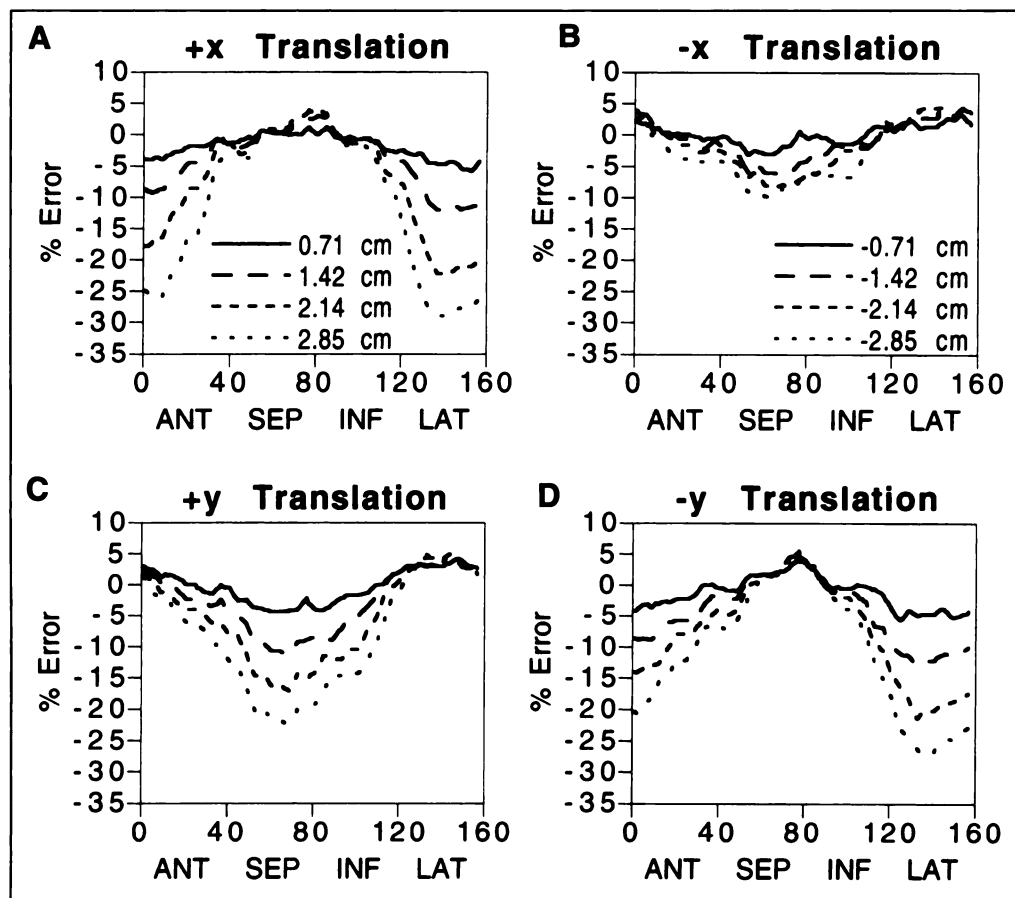

FIGURE 4. Average normalized error with the phantom for positive x-axis shift (A), negative x-axis shift (B), positive y-axis shift (C) and negative y-axis shift (D). Note: Legend in A also applies to C and legend in B also applies to D.
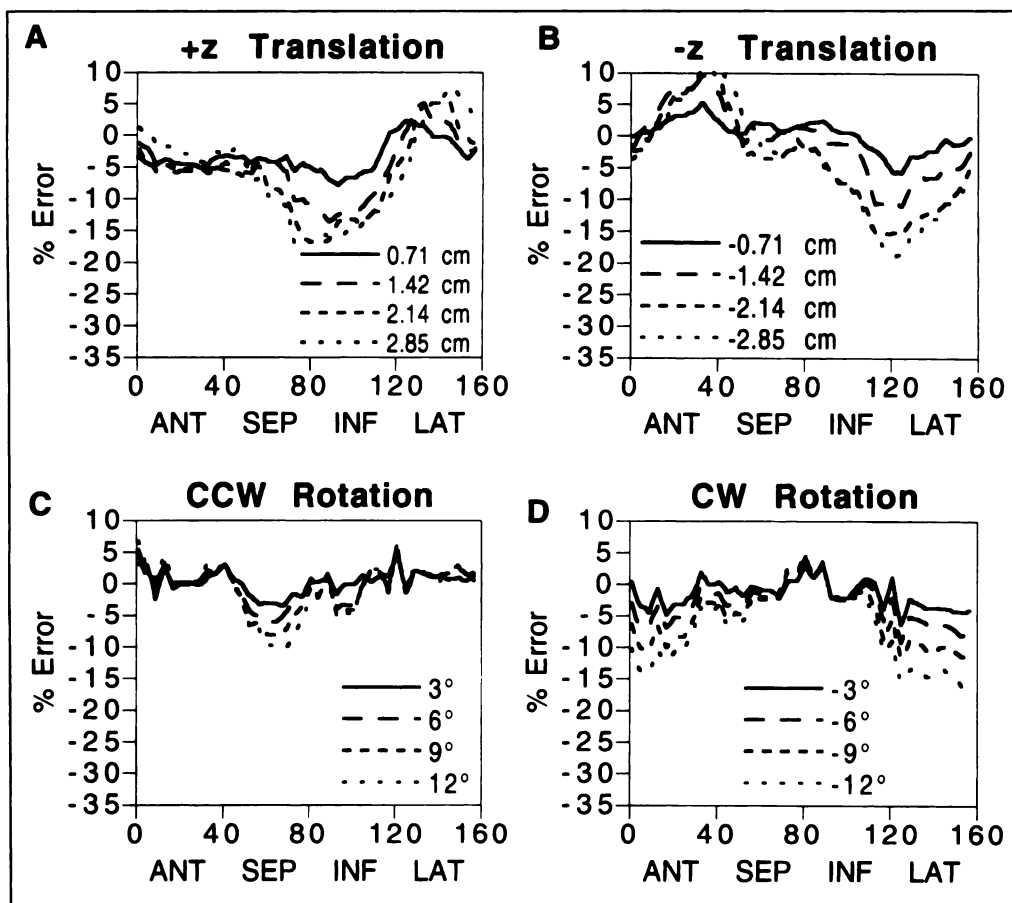
FIGURE 5. Average normalized error with the phantom for positive z-axis shift (A), negative z-axis shift (B), counterclockwise rotation (C) and clockwise rotation (D).

to the attenuation map. Thus, the overall image will have errors both from rotation but also from translation.

For all three experiments, the shapes of the error curves associated with each type of motion were very similar. Figure 6 shows the errors associated with each experiment for a +2.85 cm movement in the x direction. However, the magnitude of the errors varies. Table 1 compares the maximum normalized error between the three phantom experiments for the four types of misalignment. Experiment 1 contained a gap of approximately 2 cm between the heart and the lung, whereas in Experiment 2, the heart was pressed against the lung along most of its length. In Experiment 3, only an area near the apex of the heart was touching the lung. The values in Table 1 reflect the percentage errors that occurred when the heart moved over the lung boundary. This error can be as great as when no attenuation correction is performed.

Patient

For the human data, the results correspond to the phantom experiments very well. Figure 7A displays the values in the 10-pixel strip for the attenuation-corrected and uncorrected images. Figure 7B shows the error between the attenuation-corrected and uncorrected images. Comparison to Figure 3B reveals a similar shape in the error plot, with most of the error falling in the inferior region.

Figure 8A and B, displays the errors for translation along the x-axis. It can be noted that the graphs in Figure 8A and B, were qualitatively the same as those in Figure 4A and B. The main difference was the magnitude of the errors, which was for the average of all phantoms. For these data, the errors were very similar to the phantom of Experiment 2 (heart along the lung wall), and the similarity was confirmed by comparing the human patient results in Figure 8A to the errors given for Experiment 2 in Figure 6. Due to her small size, this patient's

heart was in close proximity to the lung boundary, which is similar to Experiment 2.

After the image of the human patient was compared to the phantom images along with the results from above, it was clear that the human heart is in close proximity to the lung boundary. This geometry is similar to the scenario of Experiment 2.

The errors generated for movement along the y-axis are displayed in Figure 8C and D. These errors also agree qualitatively with the errors from the phantom studies (Fig. 4C and D). The errors are greater by approximately 5%–10%.

Figure 9A and B, highlight the errors for movement along the z-axis. Figure 9A shows qualitative error similar to that of the phantom (Fig. 5A); however, movement for the human patient created larger errors. Parts of the error curves in Figure 9B were similar to those of Figure 5B, but the anterior section of the heart in the patient had large errors as it was moved. These errors were probably due to axial differences of structures within the thorax, when compared to the phantom.

The effects of rotation are illustrated in Figure 9C and D. The error curves for the rotation were, once again, qualitatively similar to those of Figure 5C and D. The only significant difference was the magnitude of error.
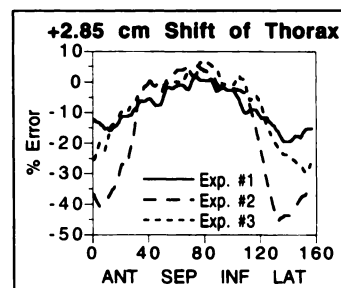

FIGURE 6. Errors associated with each phantom experiment with a positive 2.85-cm x-axis shift.

TABLE 1
Maximum Normalized Percentage Error (%) for the Three Phantom Experiments and the Human Experiment

| | Translation (2.9 cm) | | | | | | Rotation (12°) | |
	+x-axis	−x-axis	+y-axis	−y-axis	+z-axis	−z-axis	CCW	CW
PE 1	−19.5	−8.6	−18.3	−18.9	−10.2	−14.3	−10.9	−15.3
PE 2	−45.3	−11.9	−27.2	−40.5	−22.6	−23.6	−10.3	−24.8
PE 3	−30.0	−12.5	−23.5	−21.1	−20.7	−19.7	−9.9	−13.5
HE	−37.2	−20.6	−18.7	−36.3	−31.1	−29.0	−11.6	−31.1

CCW = counterclockwise; CW = clockwise; PE = phantom experiment; HE = human experiment.

DISCUSSION

It is clear from the results that misregistration between the transmission and emission scans can cause significant artifacts when filtered backprojection is used in conjunction with the nonuniform iterative Chang method. This sensitivity to motion can be explained by considering the correction term in Equation 1 when computing $C(i,j)$. $C(i,j)$ has a large magnitude in the area of the heart, but it decreases rapidly as the lungs are approached. For even small offsets, the values of $C(i,j)$ will change by a large amount. In fact, the nonuniformity introduced in the image by movement under 3 cm can exceed the nonuniformity in the image reconstructed without any attenuation correction, as illustrated in the patient error curves. At present, filtered backprojection is used on the vast majority of commercial systems available in the world. Registration errors of 2 cm can cause nonuniformity artifacts that might be mistaken as an area of reduced myocardial perfusion. It appears that translation along the x-axis, y-axis or z-axis creates the greatest problems. Each type of motion considered appears to cause a nonuniform but characteristic change in the profile activity that increases monotonically with the magnitude of the misalignment. Because the artifacts manifest themselves in different segments of the heart, depending on the type of motion, it is difficult to identify the reduced activity as a characteristic artifact. Not surprisingly, as is the case with PET, the sharp boundaries that exist in the thorax seem to have a major influence on the magnitude of the errors. Although some movement may occur between scans, the acceptable error will be limited by the proximity of the heart and lung boundary.

For the sequential scan method to become practical in a clinical setting, where the time per patient is limited, efficient procedures must be developed to ensure image registration and also to detect the presence of movement errors. Most work on registration has been directed toward brain scans (11), in which the skull provides a well defined rigid boundary. For the thorax,

the boundary is, unfortunately, not rigid and, in fact, is constantly in motion due to respiration. However, a study of transmission/emission registration in thoracic PET found that, by careful application of laser alignment on the patient, x and y translation errors between scans could be limited to an average of 2.4 mm and 1.8 mm, respectively while rotation errors averaged 1.6° (14). Errors of this magnitude are less than the 3.56-mm pixel size used in this study and would certainly be acceptable. It is also hoped that the fast sequential acquisition method proposed previously (3) will reduce the frequency of patient motion by starting the emission scan soon after the fast transmission scan. The longer the patient has to wait between scans, the greater the chance for patient movement.

Another issue is the acquisition of transmission maps for patients without truncation becoming a factor. We are currently developing an offset fanbeam method that will largely eliminate the problem of transmission scan truncation (25,26).

Regarding detection of registration errors between the scans, one possible method involves using an external fiduciary band to provide a well-defined edge to the thorax (10). This information can then be compared with the transmission image to make sure the edges are registered. A second possible method is to determine the thorax boundary using Compton scatter data (27). Another possibility would be to perform two transmission scans, one before the emission scan and one after the emission scan. The edges in the two transmission scans could be compared to infer that patient movement during the study was unlikely.

CONCLUSION

The results indicate that registration errors of 2–3 cm between the transmission and emission scans can cause significant artifacts in the reconstructed images. These artifacts occur when using filtered backprojection in conjunction with the nonuniform iterative Chang method. Registration errors can cause nonuniformity

FIGURE 7. A 10-pixel-wide profile for the human study of the attenuation-corrected and uncorrected Mercator plots (A). Plot of the normalized error for the case in which no attenuation correction was performed on the phantom SPECT image (B).
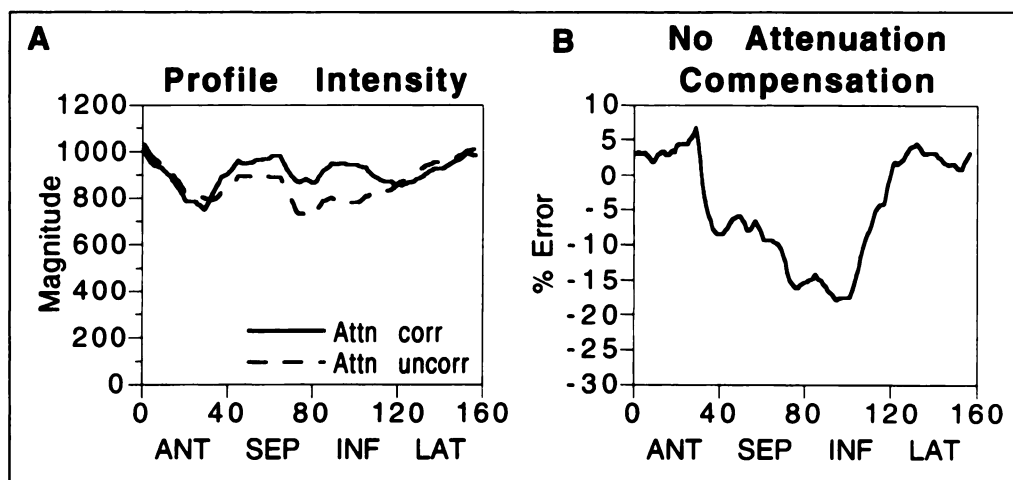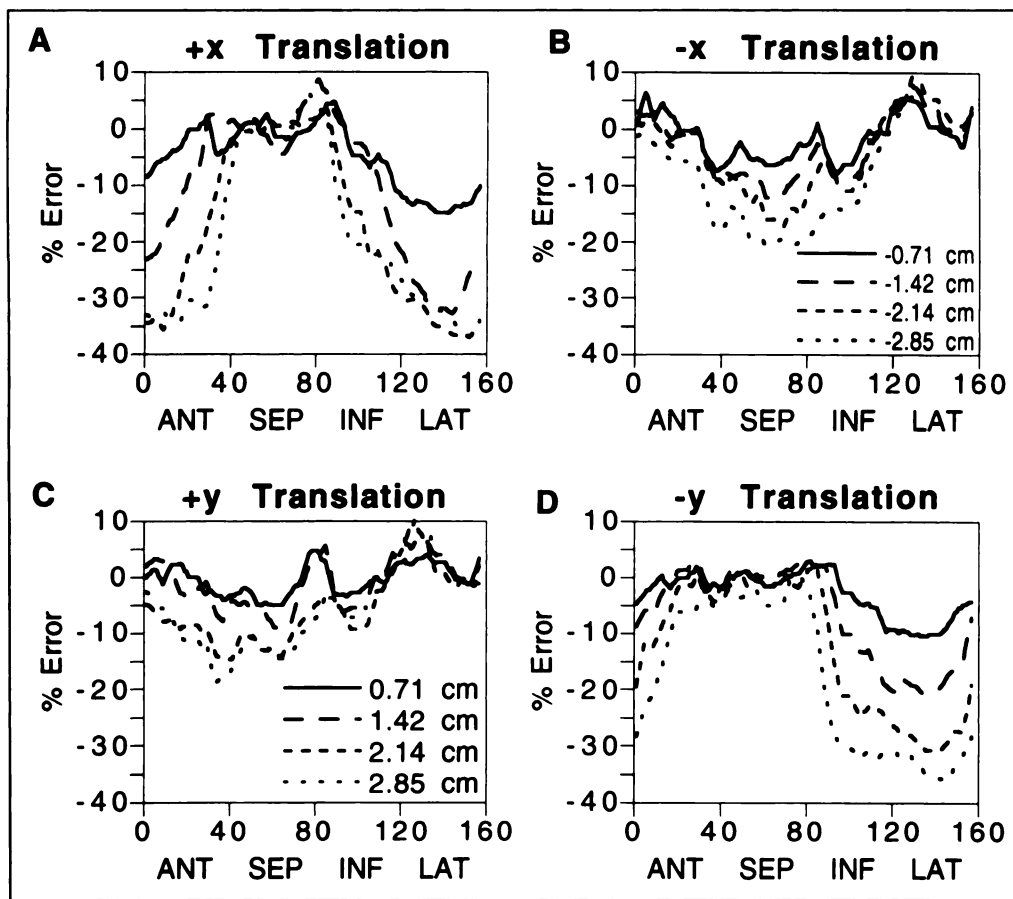
FIGURE 8. Average normalized error for the human study with positive x-axis shift (A), negative x-axis shift (B), positive y-axis shift (C) and negative y-axis shift (D). Note: Legend in C also applies to A and legend in B also applies to D.
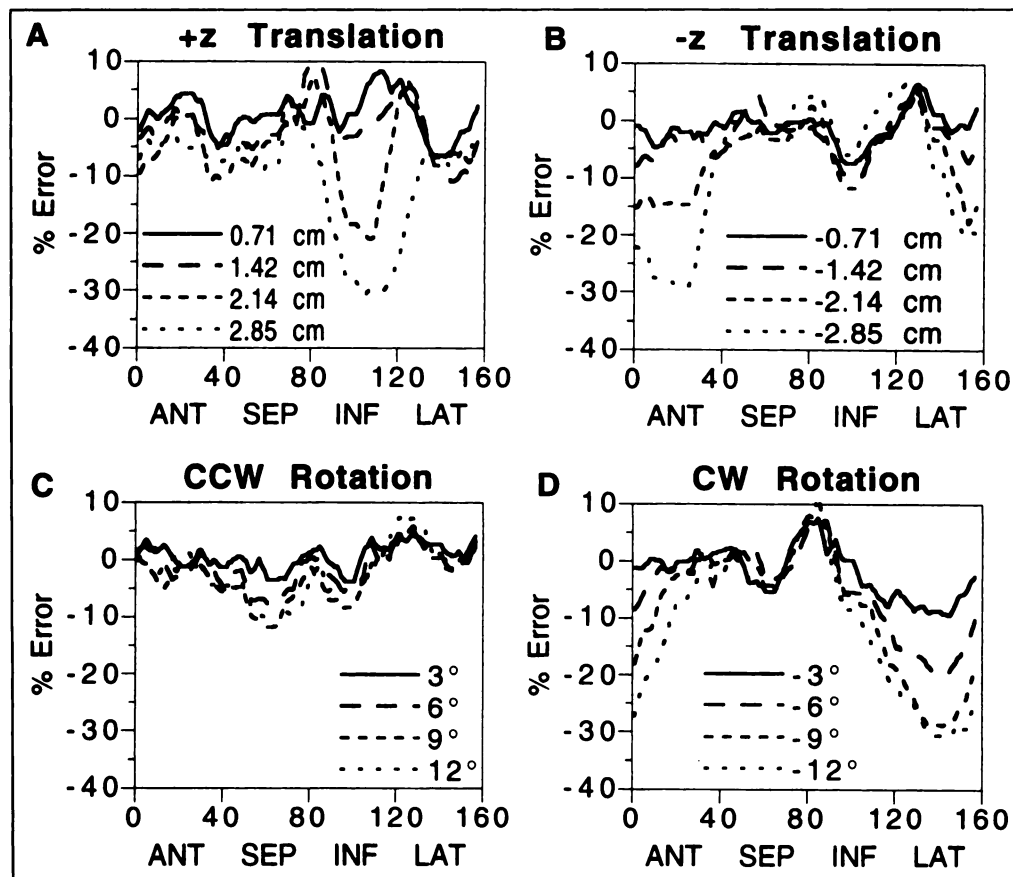

FIGURE 9. Average normalized error for human data with positive z-axis shift (A), negative z-axis shift (B), counterclockwise rotation (C) and clockwise rotation (D).

artifacts that may be interpreted as an area of reduced myocardial perfusion. Because these artifacts are direction of motion dependent in terms of the different segments of the heart, it is difficult to diagnose the reduced image count density as reduced perfusion or characteristic artifact. For the sequential scan method to become clinically acceptable, efficient procedures must be developed to ensure proper image registration.

ACKNOWLEDGMENTS

REFERENCES

1. Tsui BMW, Gullberg GT, Edgerton ER, et al. Correction of nonuniform attenuation in cardiac SPECT imaging. *J Nucl Med* 1989;30:497–507.
2. Tung CH, Gullberg GT, Zeng GL, et al. Non-uniform attenuation correction using simultaneous transmission and emission converging tomography. *IEEE Trans Nucl Sci* 1992;39:1134–1143.
3. Jaszczak RJ, Gilland DR, Hanson MW, et al. Fast transmission CT for determining attenuation maps using a collimated line source, rotatable air-copper-lead attenuators and fan-beam collimation. *J Nucl Med* 1993;34:1577–1586.
4. Manglos SH, Jaszczak RJ, Floyd CE, et al. A quantitative comparison of attenuation-weighted backprojection with multiplicative and iterative postprocessing attenuation compensation in SPECT. *IEEE Trans Med Imag* 1988;7:127–134.
5. Murase K, Itoh H, Mogami H, et al. A comparative study of attenuation correction algorithms in single photon emission computed tomography. *Eur J Nucl Med* 1987;13:55–62.
6. Wallis JW, Miller TR, Koppel P. Attenuation correction in cardiac SPECT without a transmission measurement. *J Nucl Med* 1995;36:506–512.
7. Ficaro EP, Fessler JA, Ackermann RJ, et al. Simultaneous transmission-emission thallium-201 cardiac SPECT: effect of attenuation correction on myocardial tracer distribution. *J Nucl Med* 1995;36:921–931.
8. Yu JN, Fahey FH, Gage HD, et al. Intermodality, retrospective image registration in the thorax. *J Nucl Med* 1995;36:2333–2338.
9. Eberl S, Kanno I, Fulton RR, et al. Automated interstudy image registration technique for SPECT and PET. *J Nucl Med* 1996;37:137–145.
10. Scott MS, Macapinlac H, Zhang J, et al. Image registration of SPECT and CT images

using an external fiduciary band and three-dimensional surface fitting in metastatic thyroid cancer. *J Nucl Med* 1995;36:100–103.
11. Turkington TG, Jaszczak RJ, Pelizzari CA, et al. Accuracy of registration of PET, SPECT and MR images of a brain phantom. *J Nucl Med* 1993;34:1587–1594.
12. Blankespoor SC, Wu X, Kalki K, et al. Attenuation correction of SPECT using x-ray CT on an emission-transmission CT system: myocardial perfusion assessment. *IEEE Trans Nucl Sci* 1996;43:2263–2274.
13. McCord ME, Bacharach SL, Bonow RO, et al. Misalignment between PET and transmission and emission scans: its effect on myocardial imaging. *J Nucl Med* 1992;33:1209–1214.
14. Bettinardi V, Gilardi MC, Lucignani G, et al. A procedure for patient repositioning and compensation for misalignment between transmission and emission data in PET heart studies. *J Nucl Med* 1993;34:137–142.
15. Yu JN, Fahey FH, Harkness BA, et al. Evaluation of emission-transmission registration in thoracic PET. *J Nucl Med* 1994;35:1777–1780.
16. Chang L-T. A method for attenuation correction in radionuclide computed tomography. *IEEE Trans Nucl Sci* 1978;25:638–643.
17. Kadrmas DJ, Jaszczak RJ, McCormick JW, et al. Truncation artifact reduction in transmission CT for improved SPECT attenuation compensation. *Phys Med Biol* 1995;40:1085–1104.
18. Jaszczak RJ, Gilland DR, McCormick JW, et al. The effect of truncation reduction in fan beam transmission for attenuation correction of cardiac SPECT. *IEEE Trans Nucl Sci* 1996;43:2255–2262.
19. Galt JR, Cullom SJ, Garcia EV. SPECT quantification: a simplified method of attenuation and scatter correction for cardiac imaging. *J Nucl Med* 1992;33:2232–2237.
20. Wackers FJ, Berman DS, Maddahi J, et al. Technetium-99m hexakis 2-methoxyisobutyl isonitrile: human biodistribution, dosimetry, safety, and preliminary comparison to thallium-201 for myocardial perfusion imaging. *J Nucl Med* 1989;30:301–311.
21. Manglos SH, Jaszczak RJ, Floyd CE, et al. Nonisotropic attenuation in SPECT: phantom tests of quantitative effects and compensation techniques. *J Nucl Med* 1987;28:1584–1591.
22. Jaszczak RJ, Greer KL, Floyd CE, et al. Improved SPECT quantification using compensation for scattered photons. *J Nucl Med* 1984;25:893–900.
23. Gilland DR, Jaszczak RJ, Greer KL, et al. Quantitative SPECT reconstruction of iodine-123 data. *J Nucl Med* 1991;32:527–533.
24. Geckle WJ, Frank TL, Links JM, et al. Correction for patient and organ movement in SPECT: application to exercise thallium-201 cardiac imaging. *J Nucl Med* 1988;29:441–450.
25. Gilland DR, Wang H, Coleman RE, et al. Long focal length, asymmetric fan beam collimation for transmission acquisition with a triple SPECT system. *IEEE Trans Nucl Sci* 1997;44:1191–1196.
26. Gilland DR, Jaszczak JJ, Greer KL, et al. Transmission imaging on a three-headed SPECT camera using long focal, asymmetric fan beam collimation: experimental validation. *J Nucl Med* 1998:in press.
27. Jaszczak RJ, Chang L-T, Stein NA, et al. Whole-body single-photon emission computed tomography using dual, large-field-of-view scintillation cameras. *Phys Med Biol* 1979;24:1123–1143.